3. H. B. G. Casimir, *Proc. K. Ned. Akad. Wet.* **51**, 793, (1948).
4. E. Elizalde, A. Romeo, *Am. J. Phys.* **59**, 711 (1991).
5. P. W. Milonni, M. L. Shih, *Contemp. Phys.* **33**, 313 (1992).
6. L. Spruch, *Science* **272**, 1452 (1996).
7. M. Schaden, L. Spruch, *Phys. Rev. Lett.* **84**, 459 (2000).
8. M. J. Sparnaay, *Physica* **24**, 751 (1958).
9. S. K. Lamoreaux, *Phys. Rev. Lett.* **78**, 5 (1997).
10. U. Mohideen, A. Roy, *Phys. Rev. Lett.* **81**, 4549 (1998).
11. A. Roy, U. Mohideen, *Phys. Rev. Lett.* **82**, 4380 (1999).
12. B. V. Derjaguin, I. I. Abrikosova, E. M. Lifshitz, *Q. Rev. Chem. Soc.* **10**, 295 (1956).
13. J. Blocki, J. Randrup, W. J. Swiatecki, C. F. Tsang, *Ann. Phys.* **105**, 427 (1977).
14. A. A. Maradudin, P. Mazur, *Phys. Rev. B* **22**, 1677, (1980).
15. V. B. Bezerra, G. L. Klimchitskaya, C. Romero, *Mod. Phys. Lett. A* **12**, 2613 (1997).
16. J. Schwinger, L. L. DeRaad, K. A. Milton, *Ann. Phys.* **115**, 1 (1978).
17. M. Bordag, B. Geyer, G. L. Klimchitskaya, V. M. Mostepanenko, *Phys. Rev. D* **56**, 075003 (1998).
18. A. Lembrecht, S. Reynaud, *Eur. Phys. J. D* **8**, 309 (2000).
19. G. L. Klimchitskaya, U. Mohideen, V. M. Mostepanenko, *Phys. Rev. A* **61**, 062107 (2000).
20. The restoring torque of the torsional rod increases linearly with rotation angle, whereas the torque due to electrostatic attraction from the electrode is a strongly nonlinear function of the rotation angle. As the top plate rotates closer to the electrode, the electrostatic torque increases rapidly. As a result, once the angle of rotation exceeds a threshold value, the top plate becomes unstable and spontaneously tilts all the way to touch the electrode.
21. In the bridge circuit, ac excitations of opposite phases are applied to the two bottom electrodes. The top plate is connected to the input of a charge preamplifier that is a virtual ground. The output of the charge preamplifier is fed into the input of a lockin amplifier. When the sphere is far from the top plate, the amplitudes of the ac excitations are adjusted so that the output of the preamplifier is zero. As the sphere approaches and the plate rotates in response to the attractive force, the capacitance of the top plate to the two electrodes changes and the bridge goes out of balance. The lockin output is thus proportional to the rotation of the top plate.
22. Rotation of the top plate in response to the attractive force reduces the separation between the sphere and the plate. To calculate the correction to the distance due to rotation of the plate, we extend the piezo until the sphere and the plate come into contact. As we further extend the piezo, the top plate rotates by a known amount and we record the corresponding change in the capacitance signal of the torsional device. This calibrates the capacitance change with respect to the rotation of the plate. In measuring the electrostatic force and Casimir force, we retract the piezo until the sphere separates from the plate and then reapproach the sphere to the desired distance from the top plate. From the capacitance signal, we calculate the rotation of the plate in response to the attractive force and subtract this amount from the separation between the sphere and the plate.
23. The Casimir force is negligible compared with the electrostatic force (V = 289 mV) at distances larger than 300 nm but increases rapidly at small distances. At the smallest separations (~70 nm), the Casimir force is responsible for producing up to 10% of the total rotation angle. In Fig. 2, the contributions of the Casimir force (the measurement of which is described later in the text) to the rotation angle have been subtracted, yielding the rotation produced solely by the electrostatic force. Performing this procedure increases the fitted value of z_o by ~7 nm. The validity of this procedure is justified by the consistency of the fitting results when different voltages are applied to the sphere in the electrostatic force measurement.
24. E. D. Palik, Ed., *Handbook of Optical Constants of Solids* (McGraw-Hill, New York, 1950).
25. E. M. Lifshitz, *Sov. Phys. JETP* **2**, 73 (1956).
26. S. L. Lamoreaux, *Phys. Rev. A* **59**, 3149 (1999).
27. ———, *Phys. Rev. Lett.* **83**, 3340 (1999).
28. H. G. Craighead, *Science* **290**, 1532 (2000).
29. We thank M. Schaden, L. Spruch, M. R. Andrews, D. Abusch-Magder, E. K. Chan, R. de Picciotto, C. F. Gmachl, L. N. Pfeiffer, P. M. Platzman, and N. Zhitenev for assistance and useful discussions.

4 December 2000; accepted 23 January 2001

Spherical Bilayer Vesicles of Fullerene-Based Surfactants in Water: A Laser Light Scattering Study

Shuiqin Zhou,[1] Christian Burger,[1] Benjamin Chu,[1]* Masaya Sawamura,[2] Noriaki Nagahama,[2] Motoki Toganoh,[2] Ulrich E. Hackler,[2] Hiroyuki Isobe,[2] Eiichi Nakamura[2]

The low solubility of fullerenes in aqueous solution limits their applications in biology. By appropriate substitution, the fullerenes can be transformed into stabilized anions that are water soluble and can form large aggregated structures. A laser light scattering study of the association behavior of the potassium salt of pentaphenyl fullerene ($Ph_5C_{60}K$) in water revealed that the hydrocarbon anions $Ph_5C_{60}^-$ associate into bilayers, forming stable spherical vesicles with an average hydrodynamic radius and a radius of gyration of about 17 nanometers at a very low critical aggregation concentration of less than 10^{-7} moles per liter. The average aggregation number of associated particles in these large spherical vesicles is about 1.2×10^4.

The extremely hydrophobic C_{60} fullerene can be made soluble in water by connecting it with functional chargeable groups such as carboxylic acids (*1–5*) or amines (*6–8*). Hydrophilic behavior can also be introduced by an elegant and less obvious approach, one in which polarizable phenyl groups are added to C_{60} to stabilize its anion (*9–12*). Because these compounds are composed solely of carbon and hydrogen atoms, they represent a rare example of a hydrophobic hydrocarbon ball linked to a hydrophilic ion, causing the penta-substituted fullerene to achieve a surfactant functionality, as shown schematically in Fig. 1, that is different from whole-lipid substituents (*13*). The cyclopentadienide anion has intrinsic high stability through delocalization of the negative charge toward the 50-π electron system at the bottom of the C_{60} cage. This occurs as a result of "endohedral homoconjugation" (*14*) rather than by steric protection of the cyclopentadienide anion by the phenyl substituents against the attack of water or protons (i.e., kinetic stability).

We conducted a laser light scattering (LLS) study of the association behavior of $Ph_5C_{60}K$ in water. By using a combination of static and dynamic light scattering measurements, we have determined the size of $Ph_5C_{60}K$ (in terms of both the radius of gyration and the hydrodynamic radius), the size distribution, and the shape of the associated particles. We also estimated the critical aggregation concentration and the average aggregation number of the aggregated particles. A model for the resulting aggregates is presented.

The cyclopentadienides are readily available through the fivefold addition of organocopper reagent to C_{60} (*9–12*). A tetrahydrofuran (THF)-free aqueous solution of the fullerene cyclopentadienide was prepared under argon atmosphere by addition of a portion of the dark red THF solution of $Ph_5C_{60}K$ (3×10^{-3} mol liter^{-1}) into ultrapure water (THF:water ratio = 1:10 by volume), followed by evaporation of THF and repetition of this cycle four times. At concentrations of $C \geq 5 \times 10^{-3}$ mol liter^{-1}, a phase separation occurred, showing a turbid sample with visible solid particles so that no light scattering experiments could be carried out. At a concentration of $C = 2 \times 10^{-3}$ mol liter^{-1}, only a small amount of precipitation occurred and was removed by centrifugation (10 min at 1.5×10^4 rpm), leading to a dark red–colored clear stock solution that was used for the light scattering experiments.

A standard laboratory-built LLS spectrometer equipped with a BI-9000AT digital correlator (Brookhaven Instruments) and a Coherent diode-pumped solid-state (DPSS) model 532 laser operating at 200

---

[1] Department of Chemistry, State University of New York, Stony Brook, NY 11794, USA. [2] Department of Chemistry, University of Tokyo, Hongo, Bunkyo-ku, Tokyo 113-0033, Japan.

*To whom correspondence should be addressed. E-mail: bchu@notes.cc.sunysb.edu

mW power and 532 nm wavelength was used to perform LLS studies over a scattering angular range of 20° to 120°. About 2 ml of the $Ph_5C_{60}K$ solution was transferred to a special dust-free light scattering cell and was centrifuged at 6000 rpm (5.2×10^3 *g*) for 2 hours. The scattering cell was held in a brass thermostat block filled with a refractive index–matching silicone oil. The temperature was controlled to within ±0.05°C. The differential refractive index increment dn/dC value of $Ph_5C_{60}K$ in water was measured with a Brice-Phoenix differential refractometer (model Bp-2000-V) at a wavelength of 546 nm and ~23°C.

In a dynamic LLS experiment, the intensity-intensity time correlation function $G^{(2)}(t,q)$ in the self-beating mode is measured. $G^{(2)}(t,q)$ can be related to the electric field time correlation function $g^{(1)}(t,q)$ as

$$G^{(2)}(t,q) = A[1 + \beta|g^{(1)}(t,q)|^2] \tag{1}$$

where A is the baseline, β is a parameter depending on the coherence of the detection, and t is the delay time. $g^{(1)}(t,q)$ is further related to the characteristic linewidth (Γ) distribution $G(\Gamma)$ by

$$g^{(1)}(t,q) = \int_0^\infty G(\Gamma)\exp(-\Gamma t)\,d\Gamma \tag{2}$$

$G(\Gamma)$ can be calculated by a Laplace inversion of $g^{(1)}(t,q)$ using the CONTIN program (*15*). The first and second moments of $G(\Gamma)$ are $\langle\Gamma\rangle = \int_0^\infty \Gamma\, G(\Gamma)\, d\Gamma$ and $\mu_2 = \int_0^\infty (\Gamma - \langle\Gamma\rangle)^2\, G(\Gamma)\, d\Gamma$, respectively. The value of $\mu_2/\langle\Gamma\rangle^2$ is a measure of the polydispersity. If the relaxation is diffusive, Γ can be related to the translational diffusion coefficient D as

$$\Gamma/q^2 = D(1 + k_dC)(1 + f + \langle R_g^2\rangle q^2) \tag{3}$$

where k_d is the diffusive second virial coefficient, R_g is the radius of gyration, and f is a dimensionless number related to hydrodynamic draining, internal motion, polydispersity, and solvent quality (*16*). If the translational diffusion coefficient D is known, the hydrodynamic radius R_h can be obtained from the Stokes-Einstein equation

$$R_h = \frac{k_BT}{6\pi\eta D} \tag{4}$$

where k_B is the Boltzmann constant, T is absolute temperature, and η is the solvent viscosity.

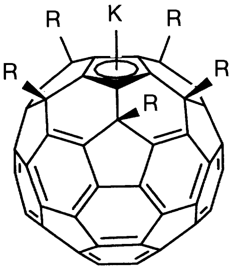

Fig. 1. Chemical structure of the penta-substituted fullerene potassium salt. In the present work, only the compound with R = Ph (= C_6H_5) has been studied.

Static LLS measures the angular dependence of the excess absolute time-averaged scattered intensity, known as the excess Rayleigh ratio $R_{vv}(q)$. In the limit of a dilute solution, the reciprocal $R_{vv}(q)$ follows the relationship

$$\frac{HC}{R_{vv}(q)} \approx \frac{1}{M_w}\left(1 + \frac{\langle R_g^2\rangle}{3}q^2\right) + 2A_2C \tag{5}$$

where $H = 4\pi^2 n^2 (dn/dC)^2/(N_A\lambda^4)$, $q = 4\pi n\lambda^{-1}\sin(\theta/2)$, n is the solvent refractive index, dn/dC is the specific refractive index increment, N_A is Avogadro's number, λ is the wavelength of the incident beam in vacuo, θ is the scattering angle, M_w is the weight-average molar mass, and A_2 is the second virial coefficient.

Figure 2 shows the apparent hydrodynamic radius ($R_{h,app}$) distributions as obtained from dynamic LLS of the $Ph_5C_{60}K$ aqueous solutions at different concentrations and at different scattering angles. At a highly dilute concentration of $C = 1 \times 10^{-7}$ mol liter^{-1}, the scattered intensity was so low that only one measurement at a scattering angle of 20° was performed.

At a concentration of $C = 2 \times 10^{-3}$ mol liter^{-1} (Fig. 2A), the size distribution consists of only one large peak with an average hydrodynamic radius $\langle R_h\rangle$ of about 16.5 nm and a polydispersity of $\mu_2/\langle\Gamma\rangle^2 \approx 0.32$, which is fairly broad. The size and the size distribution do not show an apparent angular dependence.

For diluted solutions, similar results were observed. At $C = 2 \times 10^{-6}$ mol liter^{-1} (Fig. 2B), the size distribution peaked around $\langle R_h\rangle \approx$ 17.5 nm with $\mu_2/\langle\Gamma\rangle^2 \approx$ 0.15 to 0.20, again with no apparent angular dependence. Furthermore, a very small peak around $\langle R_h\rangle \approx 1$ nm appeared in the size distribution that could possibly be attributed to dissociated $Ph_5C_{60}^-$ unimers. At $C = 1 \times 10^{-7}$ mol liter^{-1} (Fig. 2C), a size distribution with $\langle R_h\rangle \approx 16.9$ nm and $\mu_2/\langle\Gamma\rangle^2 \approx 0.12$ was observed, together with a small rudiment of "unimers." These results were reproducible after the $Ph_5C_{60}K$ aqueous solutions were settled at room temperature for 1 month.

The results from dynamic LLS can be summarized as follows: The $Ph_5C_{60}^-$ anions are associated into large aggregates with an average hydrodynamic radius of ~17 nm. This aggregation behavior is essentially independent of the concentration and occurs even in a very dilute solution of $C = 1 \times 10^{-7}$ mol liter^{-1}.

To perform the static LLS measurements, we measured the differential refractive index increment dn/dC of $Ph_5C_{60}K$ in water over a concentration range of 4.6×10^{-4} to 7.6×10^{-4} g ml^{-1} at a wavelength of 546 nm and at room temperature. A large dn/dC of −0.234 ml g^{-1} was obtained. A Zimm plot is shown in Fig. 3 over a scattering angular range of 30° to 120° and a concentration range of 1.4×10^{-6} to 2.3×10^{-6} g ml^{-1} at 25°C. From the extrapolations of $\lim_{\theta\to 0, C\to 0} HCR_{vv}^{-1}(\theta)$, we determined the weight-averaged molar mass $M_w = 1.4\ (\pm 0.2) \times 10^7$ g mol^{-1}, the radius of gyration $R_g = 17.3\ (\pm 2.5)$ nm, and a second virial coefficient $A_2 = -6.5\ (\pm 2.0) \times 10^{-10}$ ml mol g^{-2}.

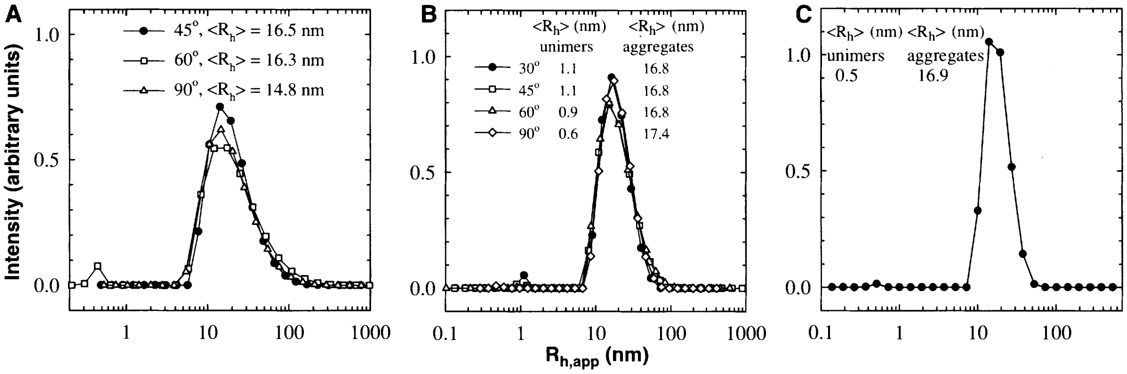

Fig. 2. Apparent hydrodynamic radius distributions of $Ph_5C_{60}K$ in water. (**A**) $C = 2 \times 10^{-3}$ mol liter^{-1}, dark red color; (**B**) $C = 2 \times 10^{-6}$ mol liter^{-1}, colorless; (**C**) $C = 1 \times 10^{-7}$ mol liter^{-1}, colorless.

Atomic force microscopy measurements (*17*) of the same system showed the aggregates to be spherical in shape, with the same radius (~17 nm). For solid spheres, the ratio of radius of gyration to hydrodynamic radius, R_g/R_h, is about 0.774. A value of R_g/R_h close to unity

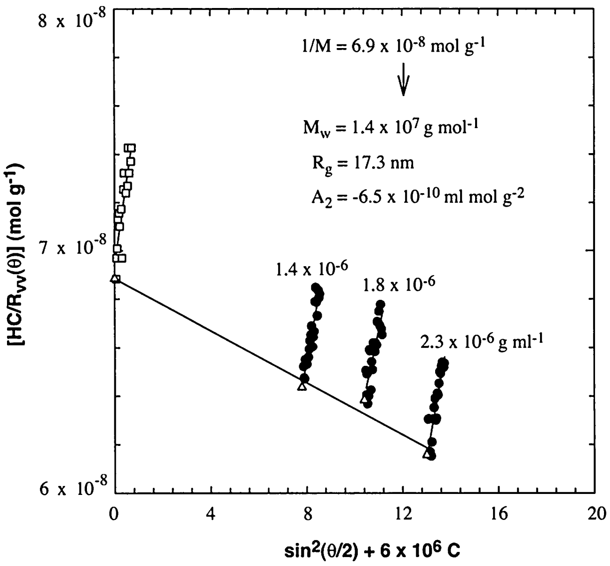

Fig. 3. Zimm plot of $Ph_5C_{60}K$ in water, obtained at $T = 25°C$ over a concentration range of 1.4×10^{-6} to 2.3×10^{-6} g ml^{-1}.

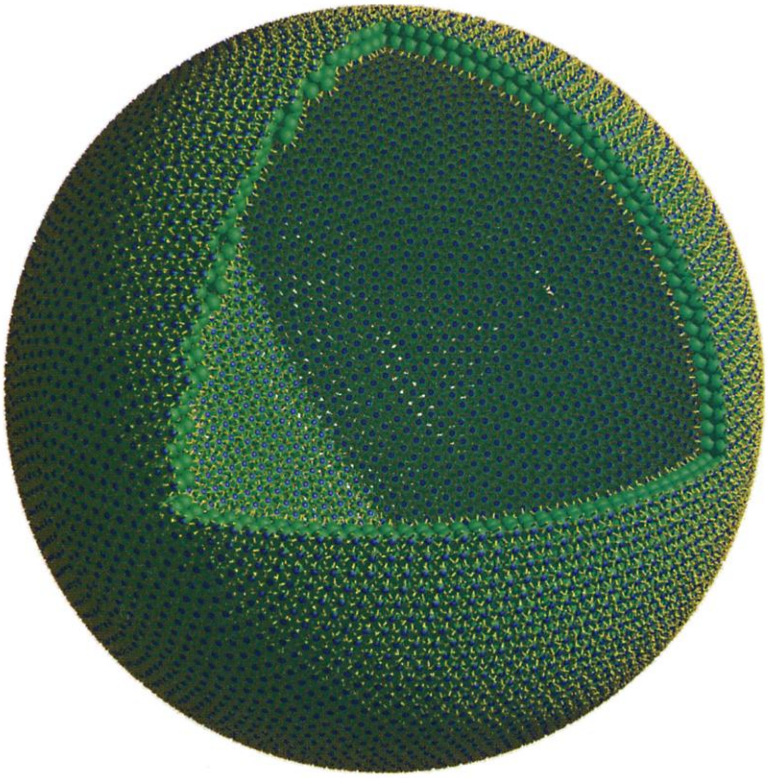

Fig. 4. A bilayer vesicle model, consisting of $N_{outer} = 6693$ molecules in an outer shell of radius $R_{outer} = 17.6$ nm plus $N_{inner} = 5973$ molecules in an inner shell of radius $R_{inner} = 16.7$ nm. A sector has been cut out for enhanced visibility. The hydrophobic fullerene bodies are shown in green, the hydrophilic-charged cyclopentadienide regions are in blue, and the five substituents are schematically represented as yellow sticks.

suggests the presence of spherical shells.

Information on M_w, R_g, and R_h of the aggregates, together with the molecular weight of the modified fullerene, enables us to develop the following model: Let us first estimate the average aggregation number N (i.e., the average number of single $Ph_5C_{60}^-$ anions per aggregate). The molecular mass of a single $Ph_5C_{60}^-$ ion is $M = 1105$ g mol^{-1} (where we have assumed that the K^+ cations are dissociated, but even if they are localized in or near the aggregates, the error should be small). Together with M_w of the aggregate $= 1.4 \times 10^7$ g mol^{-1}, the average aggregation number should be $N = M_w/M = 1.27 \times 10^4$. By assuming the thickness of the shell of a hollow sphere to be small with respect to its radius, we consider a hollow sphere of radius $R \approx R_g$. In the limit of an infinitely thin shell, this approximation would be exact. Evenly distributing $N = 1.27 \times 10^4$ molecules in the surface of such a spherical shell with a radius of $R = 17.3$ nm provides an average area of 0.296 nm^2 per molecule, not enough for a fullerene. Thus, if the aggregate is a hollow sphere, its shell could be composed of several layers stacked in an onion-like fashion. By considering the spherical shell to be a bilayer and neglecting the difference between the inner and the outer radius, $R_i \approx R_o \equiv R \approx R_g$, the average area per molecule is 0.592 nm^2, twice the value of the single layer. Assuming a two-dimensional hexagonal arrangement of the fullerene bodies inside a single layer leads to a distance of 0.83 nm between two individual molecules. Experimental studies of Langmuir-Blodgett films formed by carboxylic acid–substituted C_{60} molecules (*18*) resulted in an average area per molecule of 0.78 nm^2 and an interfullerene distance of 0.95 nm, both in good agreement with our calculated values. Within all the approximations involved, a bilayer vesicle (Fig. 4) can satisfy all the experimental observations and parameters.

On the basis of experimental values for M_w, R_g, R_h, the aggregation number N, and the aggregate shape as well as the known size of C_{60}, we have shown that $Ph_5C_{60}K$, a modified fullerene molecule, can self-assemble to form unique bilayered vesicles. In contrast to lipid membranes or liposome vesicles, the well-defined fullerene-based "surfactants" have a distinct feature: Instead of the flexible hydrophobic tails, the modified C_{60} has a rigid hydrophobic ball with a dominant intrinsic geometric constraint. Furthermore, organic chemistry permits rational design on the chemical nature of these modified fullerenes, in terms of hydrophobicity (e.g., by varying the R group, as shown in Fig. 1), geometric constraint (size and shape), and charge (cationic, anionic, or neutral; univalent or multivalent) as well as spacing between the charges and the hydrophobic part. The modified fullerenes have also been found to be relatively nontoxic; that is, the toxicity does not come from the C_{60} part but from the charged (e.g., cationic) part that can be chemically removed. Because of its close control of the modified structures, this versatile synthetic vesicle-membrane system might find diverse applications in biology and medicine as an alternative to lipids and liposomes (*19*).

References and Notes

1. H. Tokuyama, S. Yamago, E. Nakamura, T. Shiraki, Y. Sugiura, *J. Am. Chem. Soc.* **115**, 7918 (1993).
2. S. Yamago *et al.*, *Chem. Biol.* **2**, 385 (1995).
3. E. Nakamura, H. Tokuyama, S. Yamago, T. Shiraki, Y. Sugiura, *Bull. Chem. Soc. Jpn.* **69**, 2143 (1996).
4. A. S. Bouterine *et al.*, *Angew. Chem. Int. Ed. Engl.* **33**, 2462 (1994).
5. Y.-Z. An *et al.*, *Tetrahedron* **52**, 5179 (1996).
6. S. Takenaka *et al.*, *Chem. Lett.* (no. 4), 319 (1999).
7. A. M. Cassell, W. A. Scrivens, J. M. Tour, *Angew. Chem. Int. Ed. Engl.* **37**, 1528 (1998).
8. H. Murakami, M. Shirakusa, T. Sagara, N. Nakashima, *Chem. Lett.* (no. 8), 815 (1999).

9. M. Sawamura, H. Iikura, E. Nakamura, *J. Am. Chem. Soc.* **118**, 12850 (1996).
10. M. Sawamura, H. Iikura, T. Ohama, U. E. Hackler, E. Nakamura, *J. Organometal. Chem.* **599**, 32 (2000).
11. M. Sawamura, M. Toganoh, Y. Kuninobu, S. Kato, E. Nakamura, *Chem. Lett.* (no. 3), 270 (2000).
12. M. Sawamura, H. Iikura, A. Hirai, E. Nakamura, *J. Am. Chem. Soc.* **120**, 8285 (1998).
13. M. Sano, K. Oishi, T. Ishi-i, S. Shinkai, *Langmuir* **8**, 3773 (2000).
14. H. Iikura, S. Mori, M. Sawamura, E. Nakamura, *J. Org. Chem.* **62**, 7912 (1997).
15. S. W. Provencher, *Makromol. Chem.* **180**, 201 (1979).
16. B. Burchard, M. Schmidt, W. H. Stockmayer, *Macromolecules* **13**, 580 (1980).
17. M. Sawamura *et al.*, *Chem. Lett.* (no. 9), 1098 (2000).
18. M. Matsumoto *et al. Langmuir* **11**, 660 (1995).
19. E. Nakamura *et al.*, *Angew. Chem. Int. Ed. Engl.* **39**, 4254 (2000).
20. Supported by NSF grant DMR 9984102 and DOE grant DEFG0286ER45237.016 (B.C.), by a Feodor-Lynen Fellowship from the Alexander von Humboldt Foundation (C.B.), and by a Monbusho Grant-in-Aid for Scientific Research on Priority Area (Innovative Synthetic Reactions) and the Japan Society for the Promotion of Science–NSF Exchange Program.

21 November 2000; accepted 8 February 2001

Nanobelts of Semiconducting Oxides

Zheng Wei Pan,[1] Zu Rong Dai,[1] Zhong Lin Wang[1,2]*

Ultralong beltlike (or ribbonlike) nanostructures (so-called nanobelts) were successfully synthesized for semiconducting oxides of zinc, tin, indium, cadmium, and gallium by simply evaporating the desired commercial metal oxide powders at high temperatures. The as-synthesized oxide nanobelts are pure, structurally uniform, and single crystalline, and most of them are free from defects and dislocations. They have a rectanglelike cross section with typical widths of 30 to 300 nanometers, width-to-thickness ratios of 5 to 10, and lengths of up to a few millimeters. The beltlike morphology appears to be a distinctive and common structural characteristic for the family of semiconducting oxides with cations of different valence states and materials of distinct crystallographic structures. The nanobelts could be an ideal system for fully understanding dimensionally confined transport phenomena in functional oxides and building functional devices along individual nanobelts.

Binary semiconducting oxides, such as ZnO, SnO_2, In_2O_3, and CdO, have distinctive properties and are now widely used as transparent conducting oxide materials (*1*) and gas sensors (*2*). For example, fluorine-doped SnO_2 film is widely used in architectural glass applications because of its low emissivity for thermal infrared heat (*1*). SnO_2 nanoparticles are regarded as one of the most important sensor materials for detecting leakage of several inflammable gases owing to their high sensitivity to low gas concentrations (*2*). Tin-doped indium oxide (In_2O_3:Sn, ITO) film is an ideal material for flat panel displays because of its high electrical conductivity and high optical transparency (*1*), and ZnO is regarded as an ideal alternative material for ITO because of its lower cost and easier etchability (*1*). The current studies of semiconducting oxides have been focused on two-dimensional films and zero-dimensional nanoparticles, which can be readily synthesized with various well-established techniques such as sputtering (for films) and sol-gel (for particles). In contrast, investigations of wirelike semiconducting oxide nanostructures are cumbersome because of the unavailability of nanowire structures.

As stimulated by the novel properties of carbon nanotubes, wirelike nanostructures have attracted extensive interest over the past decade because of their great potential for addressing some basic issues about dimensionality and space-confined transport phenomena as well as applications (*3*). Besides nanotubules (*4*, *5*), many other wirelike nanomaterials, such as carbides [SiC (*6*–*8*) and TiC (*6*)], nitrides [GaN (*9*, *10*) and Si_3N_4 (*11*)], compound semiconductors (*12*, *13*), element semiconductors [Si (*14*–*16*) and Ge (*14*)], and oxide [Ga_2O_3 (*17*) and MgO (*18*)] nanowires, have been successfully fabricated. In geometrical structures, these nanostructures can be classified into two main groups: hollow nanotubes and solid nanowires, which have a common characteristic of cylindrical symmetric cross section. Here, we report another group of distinctly different semiconducting oxide nanostructures that have a rectangular cross section, in correspondence to a beltlike (or ribbonlike) morphology. The oxides with the nanobelt morphology cover cations with different valence states and materials with different crystallographic structures, and it seems to be a common structural characteristic for the family of semiconducting oxides.

Our synthesis is based on thermal evaporation of oxide powders under controlled conditions without the presence of catalyst (*19*). The desired oxide powders were placed at the center of an alumina tube that was inserted in a horizontal tube furnace, where the temperature, pressure, and evaporation time were controlled. In our experiments, except for the evaporation temperature, which was determined on the basis of the melting point of the oxides used, we kept the following parameters constant: evaporation time, 2 hours; chamber pressure, 300 torr; and Ar flowing rate, 50 standard cubic centimeters per minute. During evaporation, the products were deposited onto an alumina plate placed at the downstream end of the alumina tube. The as-deposited products were characterized and analyzed by x-ray diffraction (XRD) (Philips PW 1800 with Cu Kα radiation), scanning electron microscopy (SEM) (Hitachi S800 FEG), transmission electron microscopy (TEM) [Hitachi HF-2000 FEG at 200 kV and JEOL 4000EX high-resolution TEM (HRTEM) at 400 kV], and energy-dispersive x-ray spectroscopy (EDS).

Thermal evaporation of ZnO powders (purity: 99.99%; melting point: 1975°C) at 1400°C for 2 hours resulted in white woollike products that formed in high yield on the surface of the alumina plate. SEM observations reveal that the products consist of a large quantity of wirelike nanostructures with typical lengths in the range of several tens to several hundreds of microm-

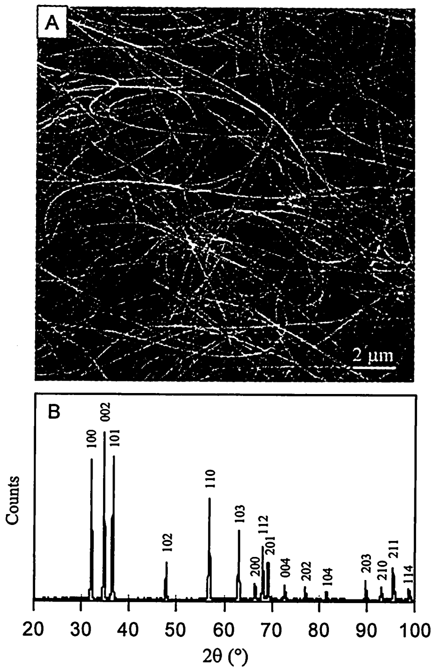

Fig. 1. Ultralong nanobelt structure of ZnO (with wurtzite crystal structure). **(A)** SEM image of the as-synthesized ZnO nanobelts obtained from thermal evaporation of ZnO powders at 1400°C. **(B)** XRD pattern recorded from the ZnO nanobelts.

---

[1] School of Materials Science and Engineering, [2] School of Chemistry and Biochemistry, Georgia Institute of Technology, Atlanta, GA 30332–0245, USA.

*To whom correspondence should be addressed. E-mail: zhong.wang@mse.gatech.edu